














RESEARCH ARTICLE | SEPTEMBER 18 2024

## Web apps for profile fitting and power balance analysis at Wendelstein 7-X



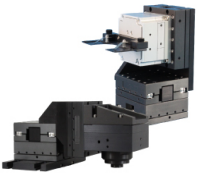
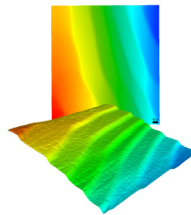
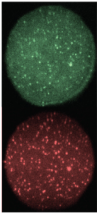
M. Wappl ; S. A. Bozhenkov ; M. N. A. Beurskens ; S. Bannmann ; M. D. Kuczyński ;  
H. M. Smith; K. J. Brunner ; O. P. Ford ; G. Fuchert ; J. P. Knauer ; A. Langenberg ;  
N. A. Pablant ; E. Pasch; P. Zs. Poloskei ; R. C. Wolf ; W7-X Team



Rev. Sci. Instrum. 95, 093529 (2024)

<https://doi.org/10.1063/5.0225315>



|  |  |  |   |  |
|--|--|--|---|--|
|  <p><b>MCL</b><br/>MAD CITY LABS INC.<br/>www.madcitylabs.com</p> | <p>Nanopositioning Systems</p>  | <p>Modular Motion Control</p>  | <p>AFM and NSOM Instruments</p>  | <p>Single Molecule Microscopes</p>  |
|--|--|--|---|--|

# Web apps for profile fitting and power balance analysis at Wendelstein 7-X

Cite as: Rev. Sci. Instrum. 95, 093529 (2024); doi: 10.1063/5.0225315

Submitted: 24 June 2024 • Accepted: 30 August 2024 •

Published Online: 18 September 2024
















View Online



Export Citation



CrossMark

M. Wappl,<sup>a)</sup>  S. A. Bozhenkov,  M. N. A. Beurskens,  S. Bannmann,  M. D. Kuczyński,  H. M. Smith, K. J. Brunner,  O. P. Ford,  G. Fuchert,  J. P. Knauer,  A. Langenberg,  N. A. Pablant,  E. Pasch, P. Zs. Poloskei,  R. C. Wolf,  and W7-X Team<sup>b)</sup>

## AFFILIATIONS

Max Planck Institute for Plasma Physics, Greifswald 17491, Germany

<sup>a)</sup> Author to whom correspondence should be addressed: [markus.wappl@ipp.mpg.de](mailto:markus.wappl@ipp.mpg.de)

<sup>b)</sup> See Grulke et al. 2024 (<https://doi.org/10.1088/1741-4326/ad2f4d>) for the W7-X Team.

## ABSTRACT

Two novel web apps for W7-X are introduced: Profile Cooker and Power House. They are designed to streamline the workflow of profile fitting and power balance analysis while offering a graphical user interface that works in any common browser. This allows us to compile a comprehensive database of experimental power balance results. All fitting functions available in Profile Cooker are presented and compared on the basis of example profiles. The power balance equation assumed in Power House is established and its individual terms are discussed. The main focus of the power balance analysis is on the turbulent transport coefficients. A model for quick calculation of neutral beam power deposition based on experimental profiles is presented. Neoclassical root transition poses an issue for power balance analysis due to the uncertainty of the radial electric field. A global, neoclassical simulation with the code EUTERPE is performed for a set of experimental profiles to gain an understanding of the neoclassical root transition.

© 2024 Author(s). All article content, except where otherwise noted, is licensed under a Creative Commons Attribution (CC BY) license (<https://creativecommons.org/licenses/by/4.0/>). <https://doi.org/10.1063/5.0225315>

## I. INTRODUCTION

To understand energy confinement and transport in a plasma, power balance analysis is a powerful tool. The global confinement of a stellarator plasma can be quickly evaluated with 0-D scaling laws, such as ISS04.<sup>1</sup> In contrast to that, power balance analysis enables a spatial resolution of confinement properties and a separation of different transport channels. The line of the analysis presented in this work resolves the power balance along a minor radius coordinate and is in that sense a 1-D approach.

A plasma can exchange power through heating, radiation, neoclassical transport, and turbulent transport. Power balance analysis puts these contributions on the balance and is essentially an experimental method. The basis is formed by one-dimensional plasma profiles of particle density and temperature, which are recorded by various diagnostics during experiments. Heating sources are either taken directly from machine parameters or calculated from the profiles by analytic models, while the radiated power can be inferred from bolometric inversions. Neoclassical transport at W7-X is well

understood by neoclassical theory, which has been verified against experimental results.<sup>2</sup> This leaves the main focus of the analysis on turbulent transport.

At Wendelstein 7-X, power balance analysis has been proven useful to investigate turbulent transport. A correlation between turbulence suppression based on observation of density fluctuations and reduced turbulent transport coefficients based on power balance analysis has been found.<sup>3</sup> In discharges with improved plasma performance after pellet injection, a reduction of heat transport to near neoclassical levels has been shown via power balance analysis.<sup>4</sup>

The aim of this work is to establish a common workflow for power balance analysis, starting from experimental data and allowing to compile a comprehensive database of power balance results comprised by a large number of experiments. The main results of the power balance analysis are the turbulent transport coefficients  $\chi_e$ ,  $\chi_i$ , and  $\chi_{\text{eff}}$ . In the following, the web apps Profile Cooker and Power House are introduced, which are designed to streamline this workflow. After that, the contributions to the power balance are covered in detail.

This paper is organized as follows: Sec. I covers the introduction. Section II provides the presentation of back- and front-end of the web apps Profile Cooker and Power House, embedding in a workflow. Section III gives the production of plasma profiles from lower level diagnostic data. Section IV presents the underlying power balance equation and derivation of turbulent transport coefficients. Section V presents the basics of neoclassical theory, neoclassical solver codes, and intricacies of the radial electric field. Section VI gives the power source and sink profiles from heating and radiation and implementation in Power House. Section VII concludes this paper.

## II. PROFILE COOKER AND POWER HOUSE

The web apps Profile Cooker and Power House are presented. They work in any common web browser and facilitate a user-friendly workflow for performing profile fitting and power balance analysis. Since the contributions to the power balance comprise

data from disperse diagnostics, the solution requires filtering and interpolation to a common radial grid. A web app offers the advantage of a standardized approach to the analysis, which reduces complexity, greatly improves efficiency, and prevents occasional human errors. It propagates measurement uncertainties in a consistent way and allows us to efficiently compile a large database of power balance analysis. In addition, it rigorously saves all inputs including raw data, calculation parameters and versions when storing the results. Figure 1 shows how Power House and Profile Cooker integrate into the existing ecosystem of web services used by the W7-X team.

Profile Cooker retrieves diagnostic data directly from the W7-X Archive.<sup>5</sup> A magnetic equilibrium is chosen from the VMEC REST API,<sup>6</sup> a web service (REpresentationalStateTransfer ApplicationProgrammingInterface) for the VMEC code.<sup>7</sup> The equilibrium is used to map the data to the minor radius. Profile fits processed by Profile Cooker are saved in a profile fits database, from where they are queried by Power House. The codes Neotransp<sup>8</sup> or NTSS<sup>9</sup> handle

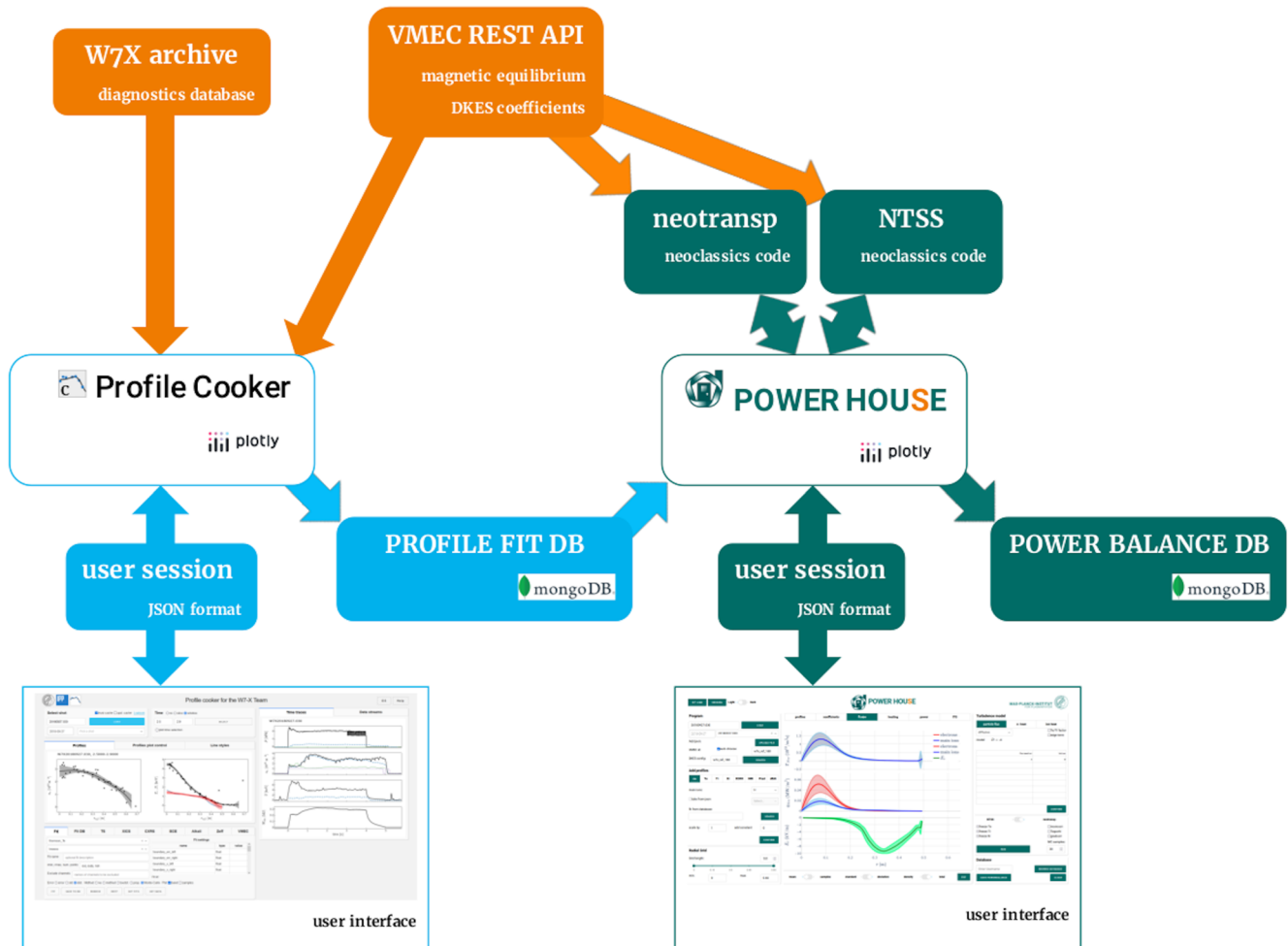


FIG. 1. Flowchart depicting the workflow with Profile Cooker and Power House.

the calculation of neoclassical fluxes, which also requires a magnetic equilibrium from the VMEC REST API. At the end of the workflow, the results of the power balance calculation are saved to a power balance database. Profile Cooker and Power House each provide a graphical user interface to handle the workflow.

### A. Back-end implementation

First of all, the back-end of the web apps is explained. The implementation of Power House is modeled after that of Profile Cooker. The following description applies to both apps. The code is written in python using dash.plotly, a handy HTML library for python.<sup>10</sup> This allows the design of a graphical user interface that works in any common browser. There are many built-in elements such as buttons, toggle switches, tabs and text entries, which can be easily programmed with callback functions. The plots are realized with the plotly framework and are fully interactive, which allows us to zoom and pan as well as to hide elements. In addition, the plots can be exported by the click of a button as either raster or vector graphics. A detailed documentation of the library is given on the plotly website.<sup>11</sup>

For the purpose of centralized storage of results, the back-end is connected to the database tool MongoDB, implemented in python with the pymongo package.<sup>12,13</sup> The user can store results in a database from where they can be reloaded and compared directly next to each other in one plot in the web app. This approach allows

us to backtrace the inputs and settings of previous calculations and to easily search and filter results. In addition to the database connection, finished work can be saved locally as a dictionary in json format if desired.

In the following, the functionality of the user interface of each tool is described.

### B. Graphical user interface of Profile Cooker

The app Profile Cooker serves as a tool for analysis and fitting of profile data at W7-X. Its use case is not limited to power balance analysis, but it serves as the foundation for many experimental studies. Figure 2 shows the graphical user interface, as seen in a web browser.

At the top, there are widgets to choose a shot and in-shot time. Once a shot is loaded, the plot widget on the right shows an overview of the time traces, including heating power, line integrated density, temperatures, and diamagnetic energy. If either a slice or window of time is selected, the respective time averaged data are displayed in the profiles plot in the center. The fits appear together with the used experimental data. All functions available in the Fit tab are explained in Sec. III. Profile Cooker optionally creates Monte Carlo (MC) samples of fits as a method to estimate the uncertainty. Previously saved fits are reloaded from a table under Fit DB. In the tab VMEC, the equilibrium used for mapping can be changed. The remaining tabs contain settings for the individual diagnostics.

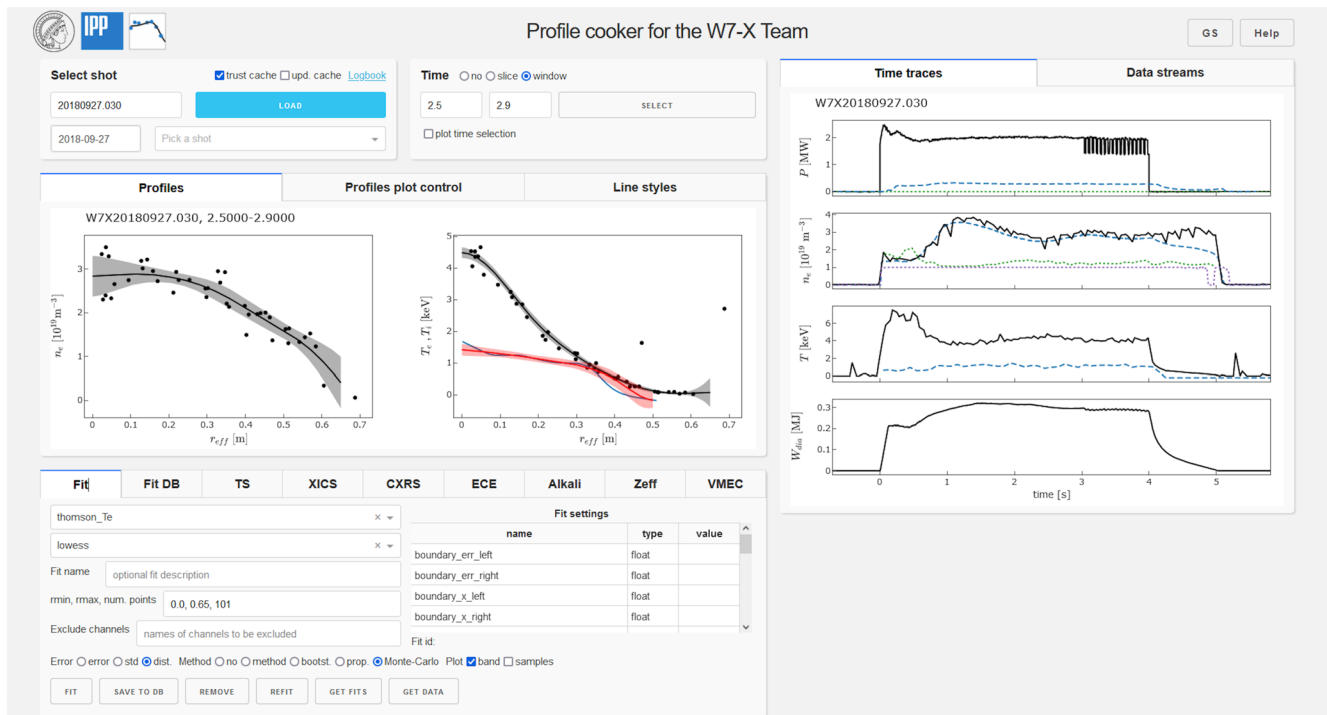


FIG. 2. Graphical user interface of Profile Cooker.

### C. Graphical user interface of Power House

Power House is a web application designed to streamline power balance analysis based on experimental plasma profiles. To this end, it is coupled to outputs of Profile Cooker. Figure 3 shows the graphical user interface.

In the Program widget, a shot number is selected. Following this, available profile fits from the fit database of Profile Cooker are chosen under the respective profiles tab. Profiles can alternatively be uploaded to Power House as a file in json format. Once profiles are added, Power House automatically chooses the best matching reference equilibrium for the data. However, it may alternatively be manually selected from a table. The main ion species in the plasma is selected in the ne tab. Since the electron density is a usual experimental input, the main ion density is adjusted to fulfill quasineutrality. At the present time, there may only be one species of ions, but an option to add plasma impurities is planned for the future.

There are further tabs with modules to add ECRH, NBI, and radiation power, as well as a kinetic energy time derivative, dEdt, which are detailed in Sec. VI. In the Radial Grid widget, the length and boundaries of the radial grid are specified, to which all input arrays as well as calculated quantities are interpolated.

Power House uses the MC samples computed by Profile Cooker to estimate the uncertainty of its fits in order to propagate errors in the power balance analysis. The number of samples taken into account can be chosen, allowing also to use sets of profiles with varying numbers of samples to be matched.

Power House is coupled to the neoclassical codes Neotransp and NTSS, which can be selected to calculate the neoclassical fluxes.

This involves finding a radial electric field  $E_r$  to satisfy the ambipolarity condition and requires a reference equilibrium and a corresponding set of transport coefficients from the DKES code.<sup>14</sup> In Neotransp, neoclassical root solutions for the electric field can be calculated separately; alternatively, a given  $E_r$  profile from a different calculation may be imported and used. NTSS does not offer these options. See Sec. V for details on the neoclassical calculation and the root solutions. The button RUN sets off the calculation.

Within the Turbulence model widget, several parametric ad-hoc models are available to estimate turbulent transport coefficients, which can be compared to the experimental findings from the power balance analysis.

The center of the user interface is occupied by a prominent plot widget. All plots are arranged in stacked triplets of related quantities. These plots serve first as a quick overview of the results, but can also be saved as raster or vector graphics for further use. An option to generate custom plots in the application will be added soon. At the bottom, there are options to display either only the quantity as a line, include an error band or the MC samples. All quantities of power may be either depicted as a local power density or cumulative integral of power, also controlled by a toggle at the bottom.

Saving and loading results from the power balance database is handled from the Database widget. It is possible to load a previous power balance calculation for editing or comparison.

### III. PROFILE FITTING

Power balance analysis requires profiles of plasma density and temperature, which means differentiable functions that can be

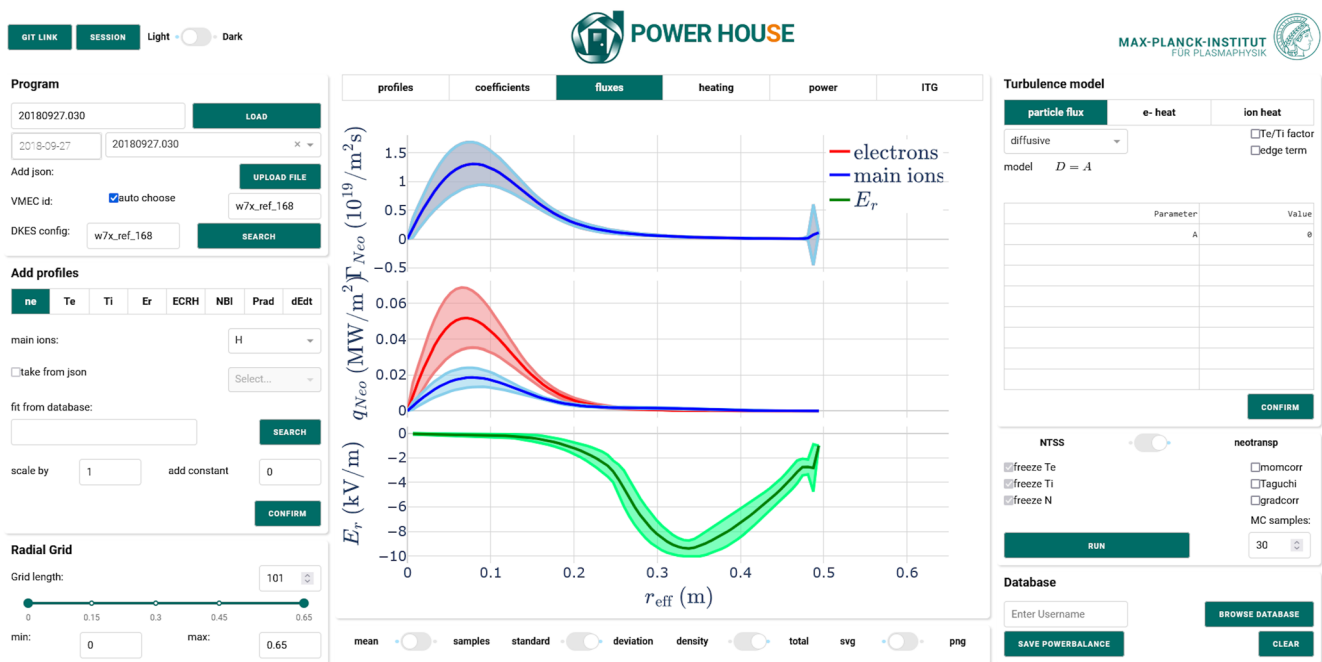


FIG. 3. Graphical user interface of Power House.

interpolated to a common, discrete minor radius grid. In a toroidal magnetic confinement device with well-defined nested flux surfaces, such as Wendelstein 7-X, an effective minor radius  $r_{\text{eff}}$  can be defined as

$$r_{\text{eff}} = a\sqrt{s}. \quad (1)$$

It serves as a flux surface label, where  $a$  is the minor radius at the last closed flux surface and  $s$  is the toroidal flux coordinate. Note that there are other, yet equivalent definitions for the effective minor radius, such as the minor radius of a torus with cylindrical cross section, major radius  $R$ , and flux surface volume  $V$ .

Plasma diagnostics measure their respective quantities either as localized data points, for instance, the Thomson scattering diagnostic<sup>15–17</sup> and the charge exchange recombination spectroscopy CXRS,<sup>18</sup> or as line integrated signals for a specific line of sight, such as the x-ray imaging crystal spectroscopy XICS.<sup>19,20</sup> The

profiles, therefore, need to be constructed as mathematical functions that match the measured data, a process called fitting.

Subsections III A–III E give an overview of the different profile fitting functions and settings offered in the fitting tool Profile Cooker. Results are compared on the basis of profile fits of two example profiles from the Thomson scattering diagnostic: an electron temperature profile from discharge W7X20180927.030 between 2.5 and 2.9 s and an electron density profile from discharge W7X20181009.016 between 4.5 and 4.7 s. Arguments are then made for the most robust and versatile function to provide sufficient accuracy in profile fitting.

### A. Fitting functions

At present, there are five different fitting functions in Profile Cooker: the polynomial, the truncated Gaussian, the two-power fit, the Gaussian process, and the lowess. Further fitting functions can be readily added thanks to the modular structure of the Profile Cooker app.

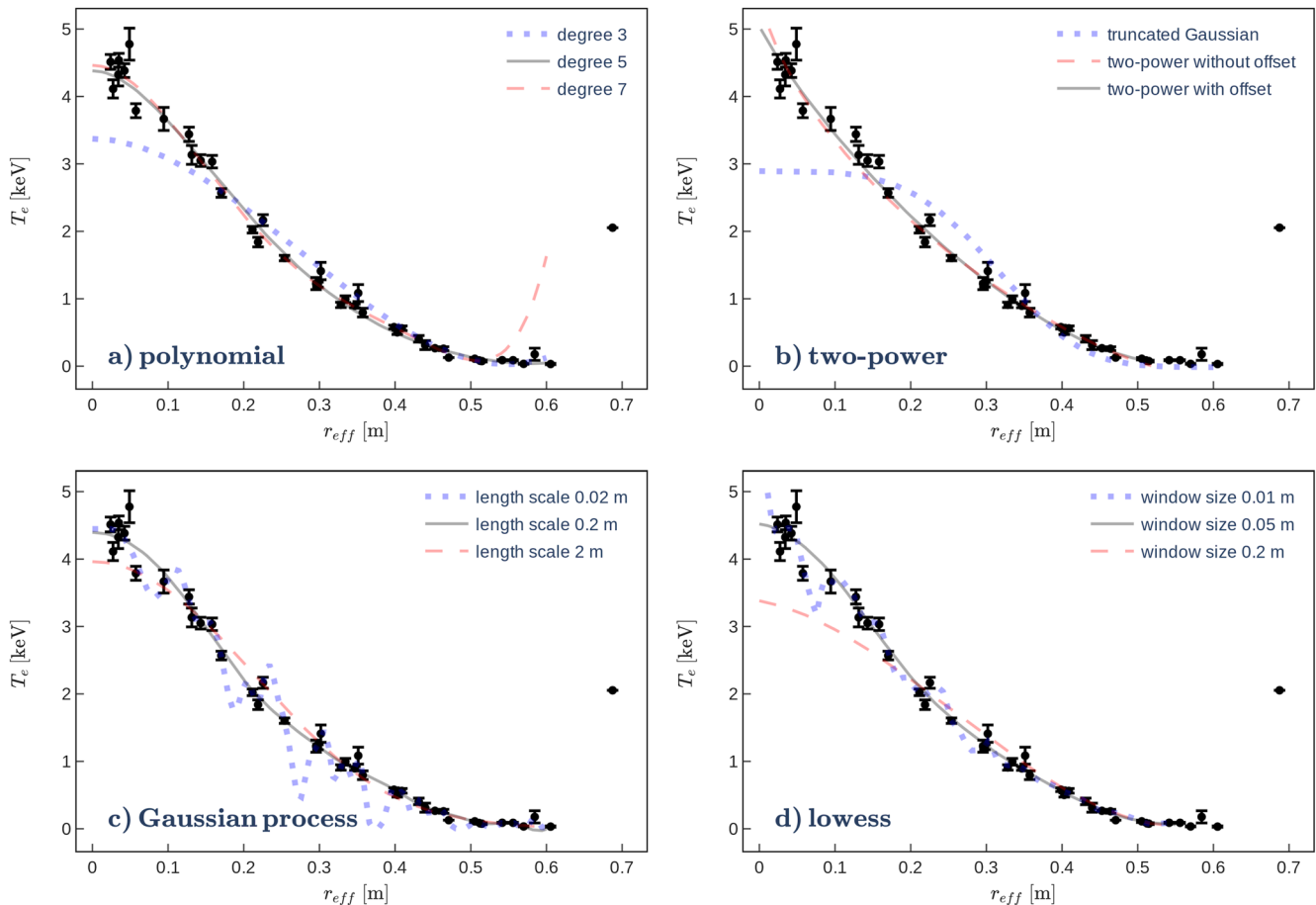


**FIG. 4.** (a) Polynomial fits with degree 3 (blue, dotted line), degree 5 (gray, solid line), and degree 7 (red, dashed line). (b) Truncated Gaussian fit (blue, dotted line), two-power fits without (red, dashed line) and with offset (gray, solid line). (c) Gaussian process fits, the length scales are 0.02 m (blue, dotted line), 0.2 m (gray, solid line), and 2 m (red, dashed line). (d) Lowess fits with a window size of 0.01 m (blue, dotted line), 0.05 m (gray, solid line), and 0.2 m (red, dashed line). Electron temperature data from the Thomson scattering diagnostic, discharge W7X20180927.030, 2.5–2.9 s.

19 September 2024 08:43:06

For the polynomial fit, the main setting is the degree of the polynomial. It must be chosen high enough to reflect the profile shape, but low enough to prevent the fit from overshooting. There is also the option to exclude the linear term, which helps eliminate a finite gradient in the center.

Truncated Gaussian fitting approximates profiles with a cut-off normal distribution function with the fit parameters  $c_0$  and  $c_1$ ,

$$f(r_{\text{eff}}) = c_0 \frac{e^{-\left(\frac{r_{\text{eff}}}{c_1}\right)^2} - e^{-\left(\frac{1}{c_1}\right)^2}}{1 - e^{-\left(\frac{1}{c_1}\right)^2}}. \quad (2)$$

This is particularly suited for profiles with a steep gradient and a plateau in the core.  $r_{\text{eff}}$  is a minor radius coordinate and  $a$  is the minor radius at the last closed flux surface.

The next fitting function is the two-power, which is well known in fusion research. It yields the three fit parameters  $c_0$ ,  $c_1$ , and  $c_2$ ,

$$f(r_{\text{eff}}) = c_0 \left( 1 - \left( \frac{r_{\text{eff}}}{a} \right)^{c_1} \right)^{c_2}. \quad (3)$$

An offset may be added to the function, which contributes a fourth parameter.

Similar to the polynomial and the truncated Gaussian, the two-power is a simple, straightforward parametric function. It works well for profiles that fall off from the plasma core to the edge with not more than one inflection point. For more complex profile shapes, the number of parameters may be insufficient for a precise regression. The lack of settings makes the truncated Gaussian and the two-power functions rather inflexible.

Gaussian process fitting is a well-known non-parametric method. In Profile Cooker, it is performed by the sklearn package, an open-source machine learning package for python.<sup>21</sup> Presently, only the radial basis function kernel (RBF) is supported in Profile Cooker. Its main setting is the length scale, which is a measure for the characteristic length on which the fit changes.

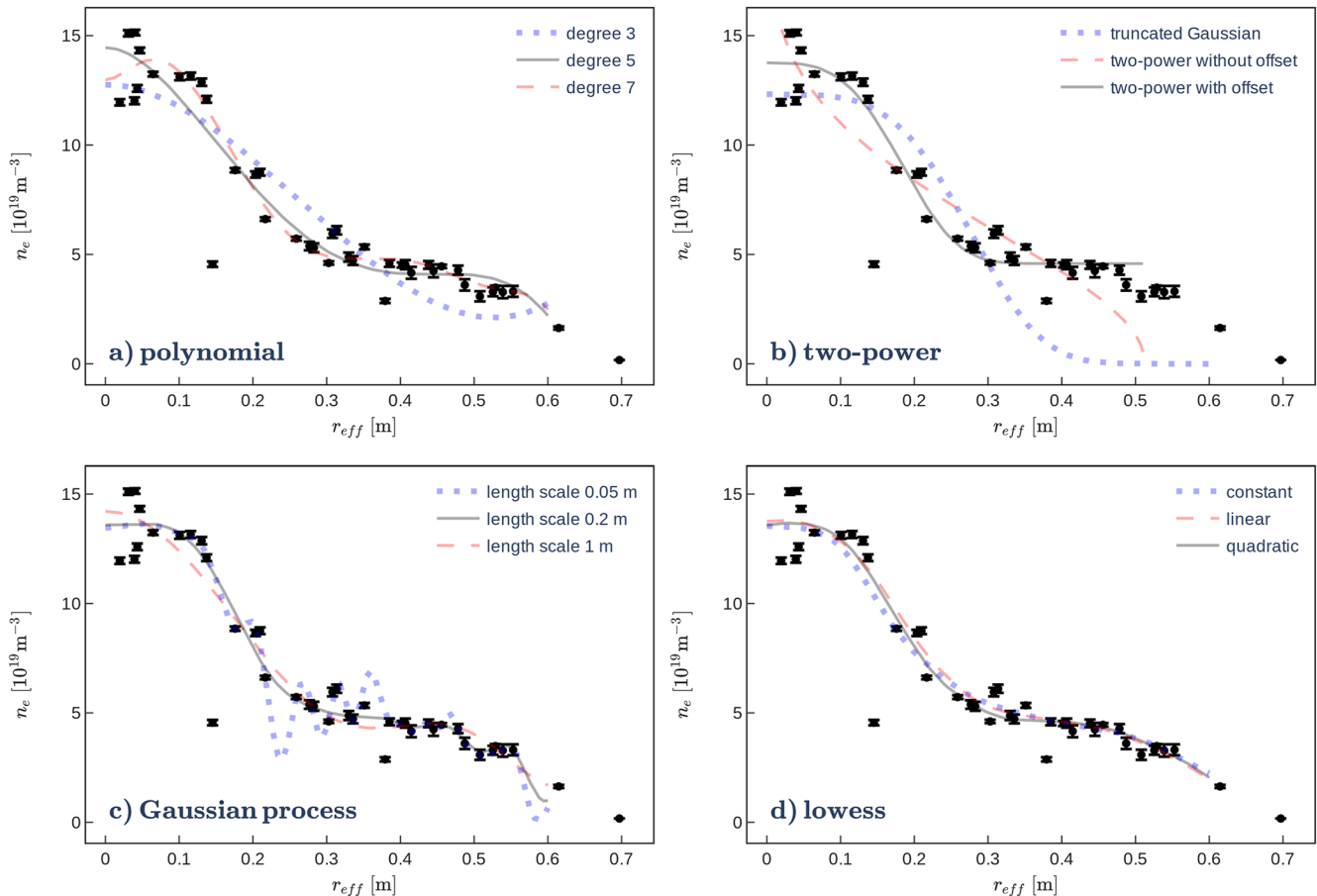


**FIG. 5.** (a) Polynomial fits with degree 3 (blue, dotted line), degree 5 (gray, solid line), and degree 7 (red, dashed line). (b) Truncated Gaussian fit (blue, dotted line), two-power fits without (red, dashed line) and with offset (gray, solid line). (c) Gaussian process fits, the length scales are 0.05 m (blue, dotted line), 0.2 m (gray, solid line), and 1 m (red, dashed line). (d) Lowess fits with the powers constant (blue, dotted line), linear (red, dashed line), and quadratic (gray, solid line). Electron density data from the Thomson scattering diagnostic, discharge W7X20181009.016, 4.5–4.7 s.

19 September 2024 08:43:06

Lowess, or loess, is a local regression that can adjust to arbitrary profile shapes. Profile Cooker uses a Nadaraya–Watson fit, which is a non-parametric regression that approximates the function locally by a polynomial. The function has two key settings, the power and the window size. The power may be constant, linear, or quadratic. The window size governs the radial range from which data points are considered for the local regression. In practice, this window size proves very helpful in making the fit either smoother or more serpentine without creating unphysical overshoots. One particular advantage of the lowess fit is its robustness against individual, outlying data points due to a leave-one-out algorithm.

The fitting functions are compared with a representative selection of parameters each for electron temperature data from W7X20180927.030 in Fig. 4 and for electron density data from W7X20181009.016 in Fig. 5.

In Sec. VII, all the fitting functions can provide reasonable results if the settings are chosen well. As non-parametric approaches, the Gaussian process and lowess are certainly more sophisticated than the parametric functions polynomial, truncated Gaussian, and two-power. As a result, they are more versatile in fitting a wide variety of profile shapes.

As the preferred function for profile fitting in this work, the lowess fit stands out. This is, first, due to its easily adjustable smoothness with the window size setting. Transport calculations as used in power balance analysis strongly depend on profile gradients, which in turn rely on smooth but precise profiles. The second reason is its robustness against outlying data points.

## B. Weighting practices for data points

Weighting refers to the relative significance that is put on data points when creating a fit, where some have more weight than others. Profile Cooker offers three weighting practices that can be selected independently of the fitting function.

First, the `error` practice performs a least square optimization with the measurement error, as provided by the respective diagnostic.

Second, the option `std` uses the standard deviation of values in a chosen time window for the least square approach. Simply phrased, the more the signal of one channel oscillates in time, the less weight is given to it for the fitting.

Third, the `dist` practice uses no errors for weighting. Instead, the scatter in the data points is taken as an error estimate, where the name `dist` refers to the distance from the fitted line. It is a particularly suitable method for profiles with unaccounted statistical errors where the data points are strongly scattered.

Figure 6 shows the comparison of different weighting practices on the basis of a lowess fit of electron density data. In this example, the measurement errors (black error bars) are not representative; thus, the weighting practice `dist` is a suitable choice.

## C. Influence of magnetic equilibrium

Diagnostics, such as Thomson scattering return data points that correspond to volumes, are located in a three-dimensional space of vessel coordinates. The transformation of these coordinates to the minor radius is called mapping and requires a 3D magnetic equilibrium reconstruction.

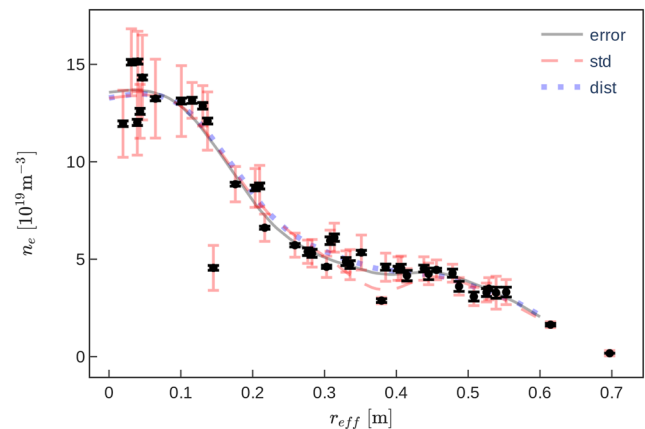


**FIG. 6.** Lowess fits with weighting practices `error` (gray, solid line), `std` (red, dashed line), and `dist` (blue, dotted line). The data points show measurement errors (black error bars) and temporal standard deviation (red error bars). From discharge W7X20181009.016, 4.5–4.7 s.

By default, Profile Cooker automatically chooses an equilibrium from a look-up table in the VMEC web API.<sup>6</sup> The parameters considered for this are the configuration (defined by the coil currents), the minor radius, and the plasma  $\beta$ . The average magnetic field on the axis is scaled to the required value. Alternatively, a specific equilibrium can be manually chosen from the VMEC web API. A plot helps compare the pressure used in the VMEC equilibrium to the kinetic pressure of the currently processed profiles.

Profile Cooker also uses ion temperatures from the x-ray imaging crystal spectroscopy XICS, which is based on line integrated measurements.<sup>22</sup> Profiles are obtained through tomographic inversion and can be found in the W7-X Archive. These profiles are, therefore, untouched by the mapping in Profile Cooker and appear as a continuous lines with error bars. The fitting works the same as for scattered data points and is performed with the same functions. Offsets may occur in the tomographic inversion, consequently the XICS tab in Profile Cooker offers input fields for scaling and offsetting the profile.

## D. Monte Carlo sampling

There are several methods for estimating the fitting uncertainties, which are selected at the bottom of the Fit tab in the Profile Cooker interface.

In the Monte-Carlo method, samples of the individual data points are generated with a distribution according to the selected weighting practice. Then, the respective fitting function is repeated for each sample, thereby creating distributed samples of the fit. The fit database then saves the value of the fit alongside with the samples. Note that the samples result from a randomized process and there is no upper or lower boundary, as the samples may cross each other. However, one can compute the standard deviation of the samples for each radial position. This may then be added to either the fit value or the mean of the samples and used as an upper or lower boundary. Power House uses three times the standard deviation as an error estimate.



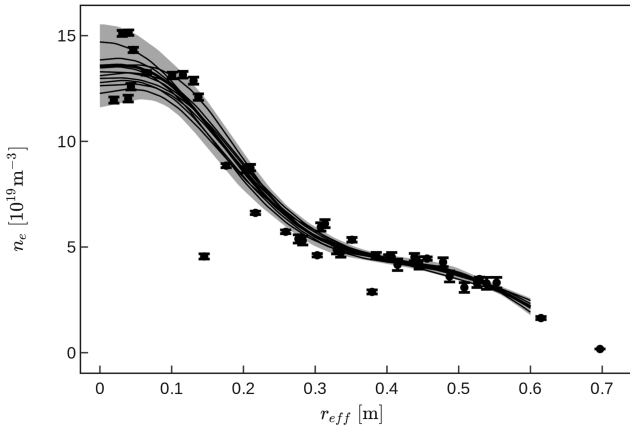


FIG. 7. MC samples of an electron density fit with uncertainty band. From discharge W7X20181009.016, 4.5–4.7 s.

The number of MC samples generated in Profile Cooker is choosable; the default is 30. Figure 7 shows a fit with 10 MC samples and an uncertainty band of twice the standard deviation, as it appears in Profile Cooker.

### E. Further settings

Profile fits are commonly demanded to have a vanishing gradient on the magnetic axis, which is motivated by the symmetry of toroidal devices. This effectively means that the derivative by the minor radius must be zero at  $r_{\text{eff}} = 0$ ,

$$\frac{d}{dr_{\text{eff}}} f(r_{\text{eff}} = 0) = 0. \quad (4)$$

To meet this, Profile Cooker offers the option `fit in s` with several of the fitting functions in Sec. III A, referring to the flux coordinate  $s$ ,

$$s(r_{\text{eff}}) = \left( \frac{r_{\text{eff}}}{a} \right)^2. \quad (5)$$

Therein, the minor radius  $r_{\text{eff}}$  is replaced by  $s$  as the x-coordinate over which the fitting is performed. The effect is illustrated on a polynomial function of degree  $n$ ,

$$f(s(r_{\text{eff}})) = \sum_{k=0}^n c_k s^k = \sum_{k=0}^n \tilde{c}_k r_{\text{eff}}^{2k}. \quad (6)$$

In the derivative, only uneven powers of  $r_{\text{eff}}$  are retained, and thus, all terms vanish for  $r_{\text{eff}} = 0$ ,

$$\frac{d}{dr_{\text{eff}}} f(s(r_{\text{eff}})) = \sum_{k=1}^n 2k \tilde{c}_k r_{\text{eff}}^{2k-1}. \quad (7)$$

Any other function may be developed into a Taylor expansion, for which the same argumentation holds. This is an easy way of ensuring a vanishing profile gradient on the magnetic axis while maintaining a smooth profile shape.

Irrespective of the chosen fitting function, core and edge boundary conditions can be set.

Profile Cooker allows the option to exclude individual data points from a profile by deselecting the respective channels. This can be done in the graphical user interface by a simple click on the point.

In addition, the lowess fitter performs automated weighting of outliers by the leave-one-out algorithm.

## IV. POWER BALANCE EQUATION

In this section, the power balance equation assumed in Power House shall be established. It is a function of a radial coordinate such that it can be solved with the input of measured 1-D plasma profiles.

The power balance equation for a plasma derives from the energy continuity equation, which has the dimension of a power density in its differential form,

$$\frac{\partial e_{\text{kin}}}{\partial t} = -\vec{\nabla} \cdot \vec{q} + p_{\text{source}}. \quad (8)$$

The temporal change of kinetic energy density  $e_{\text{kin}}$  is equal to minus the divergence of energy flux  $\vec{q}$  plus a local power density source or sink  $p_{\text{source}}$ .

To transform the power balance equation to only depend on  $r_{\text{eff}}$ , it is averaged over a flux surface. This operation entails integrating over the toroidal and the poloidal coordinate and normalizing to the surface area of the flux surface, denoted by  $\langle \cdot \rangle$ . Flux surface quantities, such as particle density  $n$  and temperature  $T$ , are constants on flux surfaces; thus, the average of  $e_{\text{kin}} = \frac{3}{2} n T$  is trivial. This is not true for the energy flux  $\vec{q}$ . Assuming that the gradient of the flux surface volume,  $\vec{\nabla} V$  exists; the flux surface averaged divergence of  $\vec{q}$  can be expressed as

$$\begin{aligned} \langle \vec{\nabla} \cdot \vec{q} \rangle &= \left\langle \frac{\partial q_k}{\partial x_k} \right\rangle = \left\langle \frac{\partial q_k}{\partial V} \frac{\partial V}{\partial x_k} \right\rangle = \left\langle \frac{\partial}{\partial V} \left( q_k \frac{\partial V}{\partial x_k} \right) \right\rangle \\ &= \frac{\partial}{\partial V} \langle \vec{q} \cdot \vec{\nabla} V \rangle = \frac{\partial r_{\text{eff}}}{\partial V} \frac{\partial}{\partial r_{\text{eff}}} \langle \vec{q} \cdot \vec{\nabla} r_{\text{eff}} \frac{\partial V}{\partial r_{\text{eff}}} \rangle \\ &= \frac{1}{V'} \frac{\partial}{\partial r_{\text{eff}}} V' \langle \vec{q} \cdot \vec{\nabla} r_{\text{eff}} \rangle = \frac{1}{V'} \frac{\partial}{\partial r_{\text{eff}}} V' q_{\text{avg}}, \end{aligned} \quad (9)$$

$$q_{\text{avg}} = \langle \vec{q} \cdot \vec{\nabla} r_{\text{eff}} \rangle, \quad (10)$$

where  $q_{\text{avg}}$  is introduced as an averaged, scalar quantity that measures the energy flux across a flux surface and the prime  $'$  denotes the partial derivative with respect to  $r_{\text{eff}}$ . In the following, any energy flux  $q$  or particle flux  $\Gamma$  is to be understood as an averaged flux by the definition of Eq. (10). This yields a one-dimensional power balance equation,

$$\frac{\partial e_{\text{kin}}}{\partial t} = -\frac{1}{V'} \frac{\partial}{\partial r_{\text{eff}}} V' q + \langle p_{\text{source}} \rangle. \quad (11)$$

In addition to this differential form with the dimension of a power density, the power balance equation can be transformed to an integral form by the volume integration  $\int_{r_{\text{eff}}=0}^{r_{\text{eff}}} V' d\tilde{r}_{\text{eff}}$ ,

$$\frac{\partial E_{\text{kin}}}{\partial t} = -qV' + P_{\text{source}}. \quad (12)$$

This quantifies the accumulated power inside the flux surface labeled with  $r_{\text{eff}}$  and is, therefore, referred to in the following as a

cumulative integral. The kinetic energy  $E_{\text{kin}}$  and the power source  $P_{\text{source}}$  result from integration over the energy density  $e_{\text{kin}}$  and the power density  $\langle p_{\text{source}} \rangle$ , respectively.

Equation (12) can be applied to a single fluid plasma or to an individual particle species like electrons. For the latter case, the contributions to the power balance equation shall be discussed in more detail,

$$\begin{aligned} \frac{3}{2} \frac{\partial}{\partial t} \int_{r_{\text{eff}}=0}^{r_{\text{eff}}} (n T) V' d\tilde{r}_{\text{eff}} &= -(q_{\text{NC}} + q_{\text{turb}}) V' \\ &+ \int_{r_{\text{eff}}=0}^{r_{\text{eff}}} Z e \Gamma_{\text{NC}} E_r V' d\tilde{r}_{\text{eff}} \\ &+ P_{\text{heat}} + P_{\text{exchange}} - P_{\text{rad}}. \end{aligned} \quad (13)$$

The energy flux  $q$  can be broken up into a neoclassical energy flux  $q_{\text{NC}}$  caused by collisions and an anomalous energy flux  $q_{\text{turb}}$  caused by plasma turbulence. The neoclassical energy flux is accompanied by a neoclassical convective flux  $\Gamma_{\text{NC}}$ , which are both well understood by neoclassical theory.<sup>2</sup>

Relevant contributions to the power source term are the externally applied heating power  $P_{\text{heat}}$ , the collisional heat exchange with other particle species  $P_{\text{exchange}}$ , and radiative losses  $P_{\text{rad}}$ . The term  $Z e \Gamma_{\text{NC}} E_r$  captures the work exerted on moving particles with charge number  $Z$  in a radial electric field  $E_r$ .<sup>9</sup>

Equation (13) provides a 1-D approach to plasma confinement, which complements the nested flux surface structure of W7-X and other magnetic confinement devices.

### A. Turbulent transport coefficients

By means of power balance analysis, the turbulent energy flux  $q_{\text{turb}}$  can be obtained from experiments. In this section, turbulent transport coefficients are defined. They serve as figures of merit for the level of turbulence suppression and facilitate comparisons between different plasma scenarios.

Heat conduction in a particle ensemble may be described by Fourier's law,

$$\vec{q} = -\chi n \vec{\nabla} T. \quad (14)$$

A diffusive approximation is chosen for turbulent transport, in accordance with other experimental works.<sup>23–25</sup> Under stationary conditions and for typical plasma profiles, the particle flux and, hence, the convective heat transport are small, which make this a valid simplification. The coefficient  $\chi$  possesses the dimension of a diffusivity. Applying the definition of a flux surface averaged flux from Eq. (10), a matching definition of a flux surface averaged  $\chi_{\text{avg}}$  is found,

$$\begin{aligned} q_{\text{avg}} &= \langle \vec{q} \cdot \vec{\nabla} r_{\text{eff}} \rangle = -\langle \chi n \vec{\nabla} T \cdot \vec{\nabla} r_{\text{eff}} \rangle \\ &= -\left\langle \chi n \frac{\partial T}{\partial r_{\text{eff}}} \vec{\nabla} r_{\text{eff}} \cdot \vec{\nabla} r_{\text{eff}} \right\rangle = -\langle \chi |\vec{\nabla} r_{\text{eff}}|^2 \rangle n T' \\ &= -\chi_{\text{avg}} n T', \end{aligned} \quad (15)$$

$$\chi_{\text{avg}} = \langle \chi |\vec{\nabla} r_{\text{eff}}|^2 \rangle. \quad (16)$$

Similarly, for  $q_{\text{avg}}$ , the suffix is dropped from  $\chi_{\text{avg}}$  in the following:

$$q = -\chi n T'. \quad (17)$$

When  $q$  is identified with the turbulent flux  $q_{\text{turb},e}$  in the power balance equation for electrons, the turbulent transport coefficient for electrons,  $\chi_e$ , can be extracted as

$$\chi_e = -\frac{q_{\text{turb},e}}{n_e T'_e}. \quad (18)$$

The same may be done for any ion species denoted with  $i$ ,

$$\chi_i = -\frac{q_{\text{turb},i}}{n_i T'_i}. \quad (19)$$

In cases where the heat exchange between plasma species cannot be reliably determined, it becomes necessary to treat the plasma as a single fluid. This is further discussed in Sec. VI C. To aid in the single fluid description, an effective turbulent transport coefficient  $\chi_{\text{eff}}$  shall be defined as

$$\chi_{\text{eff}} = -\frac{q_{\text{turb}}}{n_e T'_e + n_i T'_i}. \quad (20)$$

It is important to note that  $\chi_{\text{eff}}$  is not representative of a particular transport channel, as the driving mechanisms of turbulence for electrons and ions may be distinct. However, just like  $\chi_e$  and  $\chi_i$ , it is helpful as a measure for the general quality of turbulence suppression in a plasma scenario.

### B. Core and edge limits

This section defines limits to the radial range in which power balance analysis is reliable. Since the power balance analysis is a volumetric method, it is ill-defined near the magnetic axis ( $r_{\text{eff}} = 0$ ), where the considered volume is small. In addition, there are a number of caveats to the power balance specific to the plasma core and edge that shall be addressed in this section.

Many of the considered plasmas are heated by microwaves from the ECRH system of W7-X. It is usually tuned to be in resonance with the magnetic field on the magnetic axis. In reality, the deposition of microwave heating power is not perfectly punctual due to the Gaussian shape of the EC radiation.<sup>26</sup> Small deviations lead to widely varying power densities due to the small volume near the magnetic axis. It is, therefore, safest to limit the power balance analysis to the region outside of the deposition zone.

Symmetry demands the gradient of any profile to vanish on the magnetic axis. This presents a problem to the definition of the turbulent transport coefficients from Eqs. (18)–(20). In addition, the axis is often not covered by experimental data points with sufficient resolution. This requires external constraints on the profile fits. One possible approach is to fit profiles in a flux coordinate proportional to the square of the minor radius, which inherently forces the gradient to vanish on the magnetic axis. This approach is offered in Profile Cooker as an optional setting.

Close to the plasma edge, interactions with the neutral gas from either gas fueling or wall recycling become a sizable contribution to the power loss. Right at the plasma edge, the power is either deposited onto the island divertor of W7-X or other plasma facing components (PFCs), depending on the magnetic configuration, or radiated off by impurities in detachment cases.<sup>27</sup> The interaction with PFCs is not included in the power balance [Eq. (13)] and more difficult to model than the power balance in a fully ionized plasma.

To avoid the ECRH deposition zone and to ensure finite profile gradients, the power balance is evaluated outside of  $r_{\text{eff}} = 0.1$  m. To exclude interactions with neutral gas and PFCs as well as strong radiative losses, an outer limit is set at  $r_{\text{eff}} = 0.4$  m. The effective minor radius of W7-X extends to roughly  $r_{\text{eff}} = 0.5$  m<sup>6,28</sup> and depends on the magnetic configuration. These limits provide a conservative region to safely perform power balance analysis for most plasma scenarios at W7-X. Likewise, they open up an analytic range where the effects of different turbulence suppressing scenarios can be observed.

## V. NEOCLASSICAL SIMULATION

Neoclassical particle and energy fluxes  $\Gamma_{\text{NC}}$  and  $q_{\text{NC}}$  of a particle species are described by a diffusive approach, where both fluxes depend on the gradients of density and temperature  $n'$  and  $T'$  as well as the radial electric field  $E_r$ ,<sup>9</sup>

$$\Gamma_{\text{NC}} = -n D_1 \left[ \left( \frac{n'}{n} - \frac{Z E_r}{T} \right) + \left( \frac{D_2}{D_1} - \frac{3}{2} \right) \frac{T'}{T} \right], \quad (21)$$

$$q_{\text{NC}} = -n T D_2 \left[ \left( \frac{n'}{n} - \frac{Z E_r}{T} \right) + \left( \frac{D_3}{D_2} - \frac{3}{2} \right) \frac{T'}{T} \right]. \quad (22)$$

This form yields three transport coefficients  $D_1$ ,  $D_2$ , and  $D_3$ . It can be rewritten into a form with a transport matrix  $D$ ,

$$\begin{pmatrix} \Gamma_{\text{NC}} \\ q_{\text{NC}} \end{pmatrix} = -n T \begin{pmatrix} D_1 & D_2 \\ D_2 & D_3 \end{pmatrix} \begin{pmatrix} \frac{n'}{n} - \frac{Z E_r}{T} - \frac{3 T'}{2 T} \\ \frac{T'}{T} \end{pmatrix}. \quad (23)$$

The off-diagonal elements  $D_2$  are assumed to be equal, which is valid close to the thermal equilibrium due to the Onsager relation.<sup>29</sup>

Each of the coefficients  $D_n$  is calculated by a kinetic energy integral over a monoenergetic transport coefficient  $D_{11}$  for particles with mass  $m$  and velocity  $v$ ,<sup>9</sup>

$$D_n = \frac{2}{\sqrt{\pi}} \int_0^\infty dK e^{-K} K^{n-0.5} D_{11}, \quad K = \frac{m v^2}{2T}. \quad (24)$$

These monoenergetic transport coefficients  $D_{11}$  can, for instance, be produced by the drift kinetic equation solver code DKES.<sup>14,30</sup> They contain information on the particle drift orbits, which is the implicit cause for neoclassical transport.  $D_{11}$  is a function of three parameters with the collision frequency  $\nu$  and the average magnetic field on the magnetic axis  $B_0$ ,

$$D_{11} = D_{11} \left( r_{\text{eff}}, \frac{\nu}{v}, \frac{E_r}{\nu B_0} \right). \quad (25)$$

It is possible to compute  $D_{11}$  for a given magnetic configuration and store it as a data table for later transport calculations. There is an extensive database of reference equilibria for magnetic configurations at W7-X distinguished by coil currents and plasma  $\beta$ , each with an adjacent set of DKES data.<sup>6</sup> Power House

draws from this database and selects the most suitable dataset for a discharge.

The set of neoclassical equations is closed by the condition of ambipolarity, which determines the radial electric field  $E_r$ ,

$$\Gamma_{\text{NC},e} = Z_i \Gamma_{\text{NC},i}. \quad (26)$$

Ambipolarity links the electron flux  $\Gamma_{\text{NC},e}$  to the ion flux  $\Gamma_{\text{NC},i}$  for a charge number  $Z_i$ . It is a necessary condition to prevent the separation of electric charges and thereby violation of quasineutrality. For an axisymmetric device, neoclassical transport is inherently ambipolar.<sup>2,31</sup> In a general stellarator, on the other hand, a radial electric field arises, which enforces ambipolarity. Note that turbulent transport is generally ambipolar in the gyrokinetic approximation and, hence, does not affect the radial electric field.<sup>32</sup>

Equation (23) can be solved for an electric field  $E_r$ , on which it depends explicitly as well as implicitly through the transport coefficients  $D_n$ . There may be several solutions for the electric field; in W7-X, there are up to three.<sup>33,34</sup> These solutions are commonly referred to as roots and may exist on the entire minor radius or a limited area for a given set of profiles.

### A. Root solutions

First, the ion root is characterized by a negative value of the radial electric field. It can be illustrated as a situation where the ions would otherwise diffuse faster than the electrons, so the negative electric field restricts ion diffusion and pushes electron diffusion. The ion root is present in most W7-X discharges, at least near the plasma edge.

Second, the electron root has a positive electric field and prevails where the electron temperature is much greater than the ion temperature, which leads to a lower electron collisionality and thereby larger electron diffusion in the  $1/\nu$  regime.<sup>35</sup> These conditions are provided in the core of plasmas with low density and central electron heating, typically by ECRH.

The third root has a smaller, positive electric field and is thermodynamically unstable; thus, it is excluded from the neoclassical simulation.<sup>36</sup>

In the case that several root solutions exist for the same radial position, the electric field matches one of them and may transition to another root along the minor radius. The appearance of CERC (core electron root confinement) has been proven at Wendelstein 7-X.<sup>34</sup> Given that only the ion root solution is present at the edge of typical W7-X plasmas, a transition of the radial electric field from electron root to ion root is a necessary consequence.

The shape of the electric field in the transition area may be approximated by a diffusion equation,<sup>9</sup>

$$\frac{\partial E_r}{\partial t} - \frac{1}{V'} \frac{\partial}{\partial r_{\text{eff}}} D_E V' r_{\text{eff}} \frac{\partial E_r}{\partial r_{\text{eff}}} = \frac{|e|}{\epsilon} (\Gamma_{\text{NC},e} - Z_i \Gamma_{\text{NC},i}), \quad (27)$$

where  $D_E$  represents the diffusion coefficient for the electric field and  $\epsilon$  is the permittivity of the plasma. Qualitatively,  $D_E$  controls the width of the root transition area and thereby the steepness of the electric field, where  $D_E = 0$  forces an immediate transition with a discontinuous electric field.

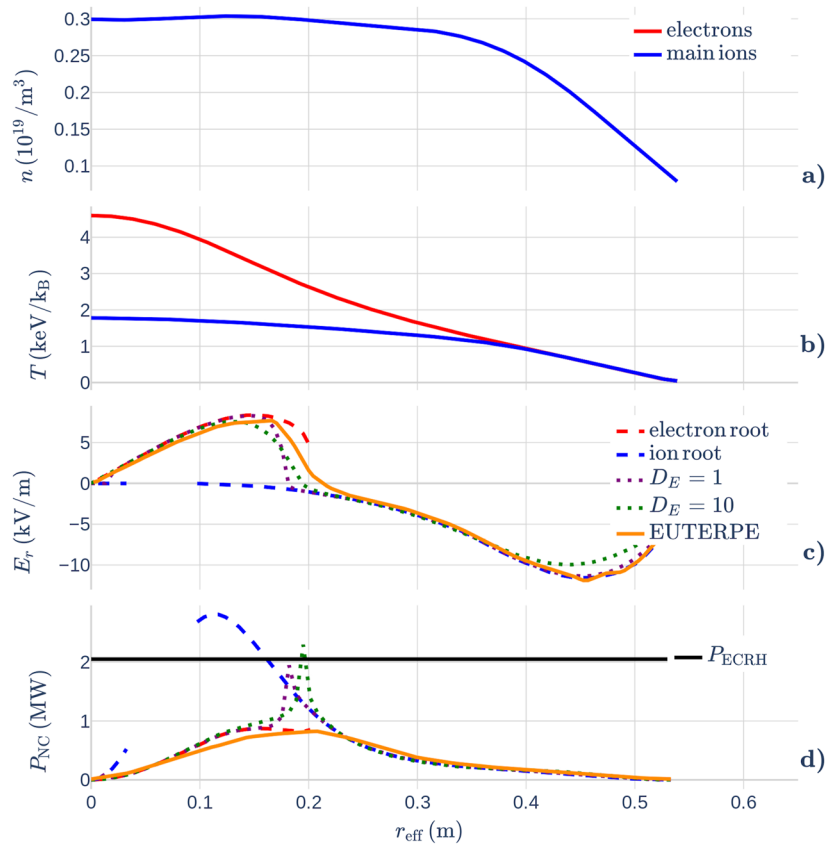


**FIG. 8.** (a) Electron and ion density (blue, solid line). (b) Electron temperature (solid, red line) and ion temperature (solid, blue line). (c) Radial electric field for electron root (dashed, red line), ion root (dashed, blue line), diffusion approximation with  $D_E = 1$  (dotted, purple line),  $D_E = 10$  (dotted, green line), and EUTERPE code (solid, orange line). (d) Cumulative neoclassical power compared to heating power from ECRH (black, solid line). From discharge W7X20221214.028, 2.5–2.9 s.

## B. Global simulations with the code EUTERPE

To evaluate the diffusion approximation in Eq. (27) for an exemplary case, a global, neoclassical simulation with the code EUTERPE was performed.<sup>37</sup> Such simulations eliminate the need for free parameters, such as the electric-field diffusion-coefficient, calculating the global electric field self-consistently with the Poisson equation instead.<sup>38</sup> Figure 8 shows a set of experimental profiles along with the radial electric field  $E_r$  and the cumulative neoclassical power  $P_{NC} = q_{NC} V'$ , as obtained by different methods.

Electron and ion root solutions as well as the diffusion approximations with  $D_E = 1$  and  $D_E = 10$  were calculated by the code Neotransp, based on monoenergetic transport coefficients obtained from the code DKES. The diffusion approximation produces an electric field gradient that matches that of the EUTERPE result for suitable  $D_E$ ; however, the exact location of the root transition ( $E_r = 0$ ) differs somewhat.

More critically, however, the diffusion approximation shows a sharp transport maximum around the location of  $E_r = 0$ , which is reflected in the cumulative power. This is likely due to the drift kinetic approximation used in the underlying DKES calculation,

which is invalid near  $E_r = 0$  and especially at low collisionality.<sup>3</sup> Using the diffusion approximation for the electric field with a DKES dataset for power balance analysis is, therefore, problematic in the transition region.

The root solutions agree well with the EUTERPE code in their respective domains, both in terms of electric field and power. The shape of the neoclassical power curve from EUTERPE suggests a smooth transition from electron root to ion root close to  $r_{\text{eff}} = 0.2$  m, unlike the transport spike found by the diffusion approximation.

Based on the comparison, the diffusion approximation can produce a reasonable electric field, while the results for the cumulative power are unreliable. Concerning power balance analysis, it is, therefore, safer to calculate the root solutions separately. Then, a continuous, smooth transition of the neoclassical power from electron root to ion root can be assumed.

## VI. SOURCE TERMS

This section shows how the different contributions of  $P_{\text{source}}$  in Eq. (12), alongside with  $\frac{\partial E_{\text{kin}}}{\partial t}$ , are being handled in the Power House app.

### A. ECRH absorption

The ECRH beam has a Gaussian power density profile.<sup>26</sup> As a rough approximation, microwave absorption may be modeled as a Gauss curve in the effective minor radius. A precise microwave power deposition profile can be attained with the code TRAVIS.<sup>4</sup> In most experiments at W7-X, the ECRH is tuned for on-axis heating. Since the power balance analysis is only considered outward of  $r_{\text{eff}} = 0.1$  m due to profile fitting, assuming the microwave power deposition to be punctual and central at  $r_{\text{eff}} = 0$  is sufficient for this case. However, some experiments are heated off-axis, where the center of power deposition is located somewhere  $r_{\text{eff}} > 0$ . For this case, Power House offers an approximation with a Gauss function with adjustable center, width, and plateau to model the ECRH power source.

There is presently no module for estimating ICRH absorption in Power House; however, a model may be developed if demand arises in the future. The main goals of the ICRH System at W7-X<sup>39</sup> are plasma start-up at a low magnetic field and studying fast ion confinement, rather than providing major heating power. Therefore, it is less relevant for power balance analysis than ECRH and NBI.

### B. NBI absorption

The power deposition of NBI is much broader than that of ECRH. Modeling of neutral beam heated plasmas, therefore, requires accurate power deposition profiles. Power House is equipped with a module for automated calculation of NBI power deposition, which takes into account neutral beam stopping through

ionization and subsequent energy transfer to electrons and ions. 3-D drift effects of fast ions are omitted.

The reaction rate of beam ionization depends locally on the density of beam and plasma, the cross section, particle species, and (explicitly and implicitly) on the beam energy. It is, furthermore, sensitive to beam parameters such as injection geometry and divergence. The NBI sources at W7-X are copies of those installed at ASDEX Upgrade, for which those parameters are documented.<sup>40,41</sup> Note that the neutral beam is not monoenergetic but consists of typically three components corresponding to the full, half, and one-third of the acceleration voltage, respectively.

After ionization, the fast ions are slowed down to thermal energy by collisions with electrons and ions. The fractions of initial beam energy heating electrons and ions can be determined as  $G_E$  and  $G_I$ ,<sup>42</sup>

$$G_E = \frac{1}{E_0} \int_{T_i}^{E_0} \frac{dE}{1 + \left(\frac{E}{E_C}\right)^{3/2}}, \quad (28)$$

$$G_I = \frac{1}{E_0} \int_{T_i}^{E_0} \frac{dE}{1 + \left(\frac{E}{E_C}\right)^{3/2}}. \quad (29)$$

These expressions are simplified for a fully ionized plasma where no re-neutralization of fast ions occurs.  $E_C$  is called the critical energy,

$$E_C = 14.8 T_e \left( \frac{A^{3/2}}{n_e} \sum_j \frac{n_j Z_j^2}{A_j} \right)^{2/3}, \quad (30)$$

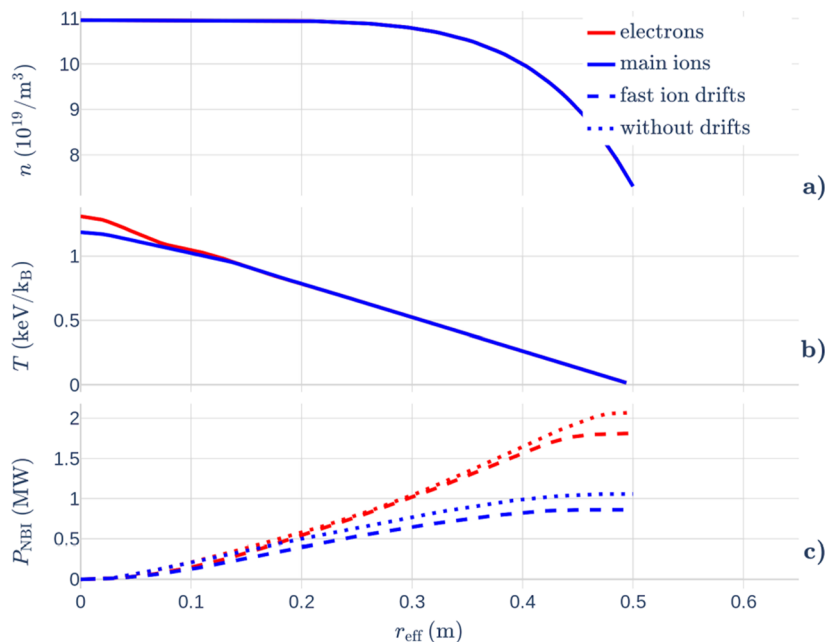


**FIG. 9.** (a) Electron and ion density (blue, solid line). (b) Electron temperature (red, solid line) and ion temperature (blue, solid line). (c) NBI power deposition with fast ion drifts from BEAMS3D on electrons (red, dashed line) and ions (blue, dashed line). NBI power deposition without fast ion drifts from the Power House beam model on electrons (red, dotted line) and ions (blue, dotted line). From discharge W7X20181009.016, 4.5–4.7 s, acceleration voltage 54 kV.

where  $T_e$  is to be entered in eV,  $A$  is the mass number of the beam particles, and  $j$  sums over the plasma ion species.

Power House makes use of a beam model that solves a collisional-radiative model based on Gaussian pencil beam geometry in order to find the birth rate of fast ions in the plasma. This model uses the Bayesian inference from beam emission spectroscopy and has been verified against other codes.<sup>18,43</sup> The same beam model has also been used in the analysis on the particle balance at W7-X.<sup>44</sup> Using a suitable equilibrium, the fast ion birth rate is then mapped to the minor radius and the fractions of power deposition calculated with Eqs. (28) and (29).

The beam model neglects drifts and losses of fast ions in the magnetic field and instead assumes a power deposition local to the ionization. Precise calculation of fast ion drifts requires a gyrocenter orbit simulation, such as the code BEAMS3D.<sup>45</sup> Figure 9 shows a comparison of the beam model in Power House against BEAMS3D for a set of example profiles along with the calculated NBI power deposition profiles.

Under consideration of fast ion drifts, the total deposited power is about 14% lower, which corresponds to the loss fraction of fast ions that leave the confined region through drifts. For the electrons, the cumulative deposited power is about 12% lower, the ions experience about 19% less power.

Codes like BEAMS3D are too computationally intensive for the workflow in Power House but can only be used as precomputed results, for example, profiles. Changes to the density profile have a profound effect on the neutral beam attenuation, which is more relevant to the power deposition than fast ion drifts. The advantage of

the beam model in Power House is that it can quickly return power deposition profiles specifically for the loaded density and temperature profiles and thereby maintain consistency. For a given discharge and time, the acceleration voltage and the intensity of each energy component of the beam are taken from the neutralizer spectroscopy of the NBI system.

### C. Collisional heat exchange

Collisional heat exchange from electrons to ions is a large uncertainty to the power balance in many cases at W7-X. This section exemplifies the reason for this and presents a reasonable way to manipulate profiles to mitigate the uncertainty.

In a plasma, the temperatures of electrons and ions are not necessarily equal. Especially in cases where only the electrons are externally heated, the difference may be significant. In this situation, the power density  $P_{\text{exchange}}$  is transferred from the electrons to the ions through Coulomb collisions,

$$P_{\text{exchange}} \sim n_e^2 \frac{T_e - T_i}{\tau_{ei}} \sim n_e^2 \frac{T_e - T_i}{T_e^{3/2}}. \quad (31)$$

It is proportional to the electron density  $n_e$  squared, the temperature difference ( $T_e - T_i$ ), and inversely proportional to the collision time  $\tau_{ei}$ . This quantity scales with  $T_e^{3/2}$ , causing the heat exchange to increase rapidly with decreasing electron temperature. Near the plasma edge,  $T_e$  tends to be very small, which leads to high exchange power density being found in Eq. (31) even for small temperature difference.<sup>3</sup>

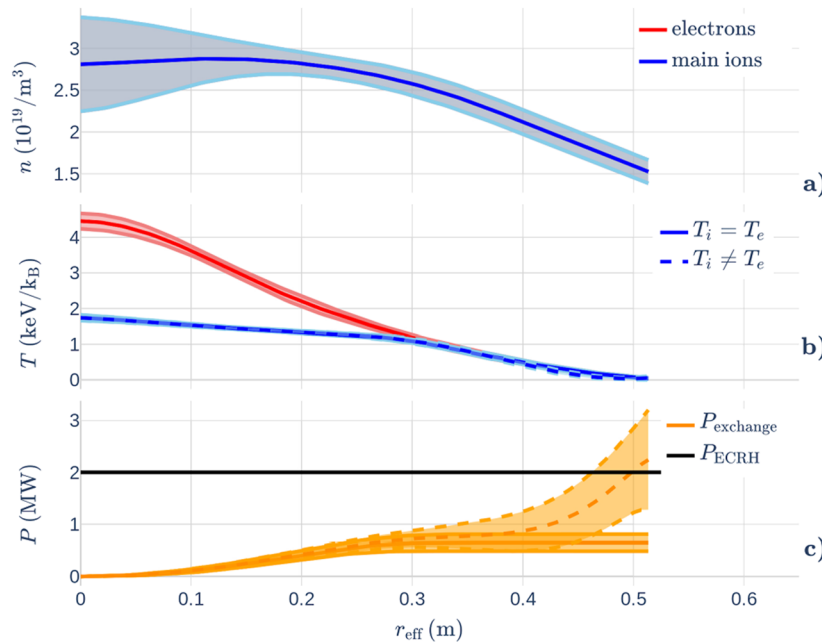


**FIG. 10.** (a) Electron and ion density (blue, solid line). (b) Electron temperature (red, solid line) and ion temperature with an initial profile (blue, dashed line) and a manipulated profile set to  $T_i = T_e$  (blue, solid line). (c) Calculated exchange power for initial profiles (orange, dashed line) and manipulated profiles (orange, solid line) compared to heating power from ECRH (black, solid line). From discharge W7X20180927.030, 2.5–2.9 s.

Figure 10 shows a set of example profiles from a stationary, pure ECRH case heated with a total of 2 MW.

There is a slight difference between  $T_e$  and the initial  $T_i$  profile (blue, dashed line) near the plasma edge. The exchange power (orange, dashed line) exceeds the total heating power of 2 MW in that area. From the standpoint of power balance, the electrons cannot dispense more power through Coulomb collisions than they receive from external heating in a stationary situation; hence, this result is paradoxical.

Physically,  $T_e$  and  $T_i$  can be assumed to be equilibrated in situations where the collision time is very short, such as for low electron temperatures near the plasma edge. Small deviations are likely due to diagnostic uncertainties. The most reasonable consequence is to set the temperatures of both species equal for the analysis, starting from a specific radius outward. Profiles manipulated by setting  $T_i$  (blue, solid line) equal to  $T_e$  from  $r_{\text{eff}} = 0.3$  m outward result in a reduced exchange power (orange, solid line).

Power House provides the option to automatically set  $T_i$  equal to  $T_e$  from the radial position where they first intersect. This may lead to a kink in the  $T_i$  profile, which is automatically smoothed by a cubic spline over adjacent data points to prevent any discontinuity in the gradient. The option is meant to mitigate an unphysical exchange power, however, it is essential for the user to oversee the result. It should be noted that in cases where the exchange power cannot be determined with confidence, the power balance must be restricted to the single fluid approximation, yielding  $\chi_{\text{eff}}$ .

#### D. Radiated power

Usually, the highest radiation densities are found at the plasma edge of W7-X.<sup>4</sup> In cases where strongly radiating impurities penetrate deeply into the plasma, they can become an important contribution to the power balance. The radiation power density can be inferred from inversions of bolometer measurements,<sup>46,47</sup> which are available in the W7-X Archive. Power House offers the option to subtract a given radiation power profile from the power balance; however, no built-in radiation model is implemented at present.

#### E. Non-stationary conditions

Power balance analysis works most reliably for plasmas where the input heating power and the density stay constant, together with the kinetic energy of the plasma. In such conditions, the profile measurements can be sampled over a long time to reduce their stochastic error and the energy derivative term  $\frac{\partial E_{\text{kin}}}{\partial t}$  is negligible. However, some plasma scenarios of particular interest, such as pellet fueling cases with improved confinement, show a highly transient character.<sup>4</sup> There, the plasma profiles and the kinetic energy may change rapidly; thus, the temporal derivative of kinetic energy must be included in the power balance.

Power House offers an application to easily add an energy derivative term. This requires sets of profiles from three or more different time points.

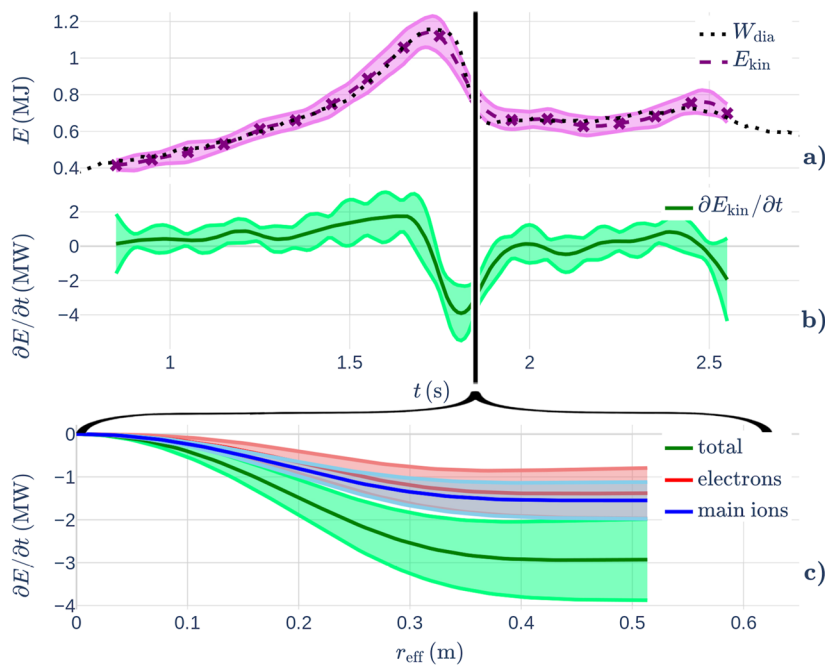


**FIG. 11.** (a) Calculated kinetic energy  $E_{\text{kin}}$  for a series of time points (purple crosses), spline interpolating these points (purple, dashed line), and measured diamagnetic energy  $W_{\text{dia}}$  for comparison (black, dotted line). (b) Time derivative of the spline (green, solid line). (c) Radially resolved kinetic energy derivative at 1.85 s as a cumulative integral, including the kinetic energy of electrons (red, solid line), ions (blue, solid line), and the single fluid plasma (green, solid line). A black, vertical bar indicates the evaluation at 1.85 s. From discharge W7X20181016.

All the profiles are interpolated to a common radial grid. For each set of profiles, the kinetic energy is calculated on the radial grid. This yields a table of kinetic energy vs time for each grid point, which is then interpolated by a cubic spline function. With that, the kinetic energy is given as a differentiable function of time that can be evaluated at any time point and for each point on the radial grid. Figure 11 visualizes the process on the basis of the pellet fueling experiment W7X20181016.037.

In Fig. 11(a), the kinetic energy  $E_{\text{kin}}$ , calculated from sets of profiles, is shown by purple crosses for a series of 18 time points. Each time point is averaged over 100 ms in this example and the profile fits consist of 30 Monte Carlo samples. The spline interpolating these points is represented by a purple, dashed line with an uncertainty interval based on the profile samples. As a proof of principle, the measured diamagnetic energy  $W_{\text{dia}}$  is plotted for comparison as a black, dotted line. In Fig. 11(b), the time derivative of the spline is shown as a green, solid line with an uncertainty interval. For demonstration, it is evaluated at 1.85 s as indicated by a black, vertical bar.

Figure 11(c) shows the radially resolved kinetic energy derivative at 1.85 s as a cumulative integral, including the kinetic energy of electrons in red, ions in blue, and the single fluid plasma in green. The integral over the effective minor radius at 0.52 m is close to  $-3$  MW; for comparison, the total heating power is 4.8 MW in this experiment. Therefore, the kinetic energy derivative term poses a non-negligible contribution to the power balance.

The accuracy of the kinetic energy calculation improves with the number and density of available time points, which requires more profile fitting and is ultimately limited by the temporal resolution of the diagnostics. In a long series of time points, the derivative is most accurate around the middle and should not be taken directly at the first or last time point. For 100 grid points and 10 time points, the computation finishes within a few seconds.

Thanks to the application described, transient plasma scenarios, such as pellet fueling cases, become accessible to power balance analysis.

## VII. CONCLUSION

Two new web apps employed at Wendelstein 7-X, the profile fitting app Profile Cooker and the power balance app Power House, are introduced. They facilitate a standardized workflow for power balance analysis and allow us to compile a large database of power balance results.

Each of the parametric and non-parametric fitting functions available in Profile Cooker are compared next to each other, in addition to weighting practices and other settings. The lowess function is preferred for its robustness and versatility.

The power balance equation, as it is assumed in Power House, is established as a function of the effective minor radius. As figures of merit, the turbulent transport coefficients  $\chi_e$ ,  $\chi_i$ , and  $\chi_{\text{eff}}$  are derived from the power balance. To avoid uncertainties, a radial range for the reliability of power balance analysis is defined as  $0.1 \text{ m} \leq r_{\text{eff}} \leq 0.4 \text{ m}$ .

The codes Neotransp and NTSS solve a set of neoclassical equations, yielding solutions referred to as electron root and ion root.

To investigate the area where a root transition occurs, a global, neoclassical simulation with the code EUTERPE was performed for an example case. It suggests a continuous, smooth transition of the neoclassical power from the electron root to ion root.

Source terms are discussed and the input options for heating power, radiative losses, and kinetic energy time derivatives in Power House are shown. The ECRH power deposition profile is approximated by a Gauss function. A beam deposition model for NBI power deposition is presented. Drifts of fast ion created by NBI are neglected and an error estimate is given. Radiative losses to the power balance may be added as a given power profile. The time derivative of kinetic energy can be computed by an application in Power House using profiles from three or more defined time points. Very small differences between electron and ion temperatures can lead to massive collisional heat exchange; thus, there is an option to manipulate  $T_i$  locally to  $T_i = T_e$ .

This work forms the basis for coming database studies on turbulent transport at Wendelstein 7-X.

## ACKNOWLEDGMENTS

This work has been carried out within the framework of the EUROfusion Consortium, funded by the European Union via the Euratom Research and Training Program (Grant Agreement No 101052200—EUROfusion). Views and opinions expressed are, however, those of the author(s) only and do not necessarily reflect those of the European Union or the European Commission. Neither the European Union nor the European Commission can be held responsible for them.

## AUTHOR DECLARATIONS

### Conflict of Interest

The authors have no conflicts to disclose.

## Author Contributions

**M. Wappl:** Formal analysis (lead); Investigation (lead); Methodology (equal); Software (equal); Visualization (lead); Writing – original draft (lead). **S. A. Bozhnikov:** Conceptualization (equal); Methodology (equal); Software (equal); Supervision (equal); Validation (lead); Visualization (equal); Writing – review & editing (lead). **M. N. A. Beurskens:** Conceptualization (equal); Methodology (equal); Supervision (equal). **S. Bannmann:** Software (equal); Writing – review & editing (equal). **M. D. Kuczyński:** Validation (equal); Writing – review & editing (equal). **H. M. Smith:** Resources (equal); Software (equal); Writing – review & editing (equal). **K. J. Brunner:** Data curation (equal); Resources (equal). **O. P. Ford:** Data curation (equal); Resources (equal). **G. Fuchert:** Data curation (equal); Resources (equal). **J. P. Knauer:** Data curation (equal); Resources (equal). **A. Langenberg:** Data curation (equal); Resources (equal). **N. A. Pablant:** Data curation (equal); Resources (equal). **E. Pasch:** Data curation (equal); Resources (equal). **P. Zs. Poloskei:** Data curation (equal); Resources (equal). **R. C. Wolf:** Supervision (lead).



## DATA AVAILABILITY

Raw data were generated at the Wendelstein 7-X facility. The data that support the findings of this study are available from the corresponding author upon reasonable request.

## REFERENCES

- <sup>1</sup>A. Dinklage, E. Ascasibar, C. D. Beidler, R. Brakel, J. Geiger, J. H. Harris, A. Kus, S. Murakami, S. Okamura, R. Preuss *et al.*, *Fusion Sci. Technol.* **51**, 1 (2007).
- <sup>2</sup>C. D. Beidler, H. M. Smith, A. Alonso, T. Andreeva, J. Baldzuhn, M. N. A. Beurskens, M. Borchardt, S. A. Bozhnikov, K. J. Brunner, H. Damm *et al.*, *Nature* **596**, 221 (2021).
- <sup>3</sup>D. Carralero, T. Estrada, E. Maragkoudakis, T. Windisch, J. A. Alonso, J. L. Velasco, O. Ford, M. Jakubowski, S. Lazerson, M. Beurskens *et al.*, *Plasma Phys. Controlled Fusion* **64**, 044006 (2022).
- <sup>4</sup>S. Bozhnikov, Y. Kazakov, O. Ford, M. Beurskens, J. Alcusón, J. Alonso, J. Baldzuhn, C. Brandt, K. Brunner *et al.*, *Nucl. Fusion* **60**, 066011 (2020).
- <sup>5</sup>M. Grahl, T. Bluhm, M. Grün, C. Hennig, A. Holtz, J. Krom, G. Kühner, H. Laqua, M. Lewerentz, H. Riemann *et al.*, *Fusion Eng. Des.* **123**, 1015 (2017), part of Special Issue: proceedings of the 29th Symposium on Fusion Technology (SOFT-29) Prague, Czech Republic, September 5-9, 2016.
- <sup>6</sup>M. Grahl, J. Svensson, A. Werner, T. Andreeva, S. Bozhnikov, M. Drevlak, J. Geiger, M. Krychowiak, and Y. Turkin, *IEEE Trans. Plasma Sci.* **46**, 1114 (2018).
- <sup>7</sup>S. Hirshman, W. van Rij, and P. Merkel, *Comput. Phys. Commun.* **43**, 143 (1986).
- <sup>8</sup>H. Smith, Neotransp, 2022.
- <sup>9</sup>Y. Turkin, C. D. Beidler, H. Maaßberg, S. Murakami, V. Tribaldos, and A. Wakasa, *Phys. Plasmas* **18**, 022505 (2011).
- <sup>10</sup>Plotly, Dash Python user guide, <https://dash.plotly.com>; accessed March 2024.
- <sup>11</sup>Plotly, Low-code Python data apps, <https://plotly.com>; accessed March 2024.
- <sup>12</sup>I. 2024 MongoDB, Mongod, <https://www.mongodb.com>; accessed March 2024.
- <sup>13</sup>I. 2024 MongoDB, Pymongo 4.6.2 documentation, <https://pymongo.readthedocs.io>; accessed March 2024.
- <sup>14</sup>S. P. Hirshman, K. C. Shaing, W. I. van Rij, C. O. Beasley, Jr., and J. Crume, *Phys. Fluids* **29**, 2951 (1986).
- <sup>15</sup>E. Pasch, M. Beurskens, S. Bozhnikov, G. Fuchert, J. Knauer, and R. Wolf, “The Thomson scattering system at Wendelstein 7-X,” *Rev. Sci. Instrum.* **87**, 11E729 (2016).
- <sup>16</sup>S. Bozhnikov, M. Beurskens, A. D. Molin, G. Fuchert, E. Pasch, M. Stoneking, M. Hirsch, U. Höfel, J. Knauer, J. Svensson *et al.*, *J. Instrum.* **12**, P10004 (2017).
- <sup>17</sup>G. Fuchert, P. Nelde, E. Pasch, M. Beurskens, S. Bozhnikov, K. Brunner, J. Meineke, E. Scott, R. Wolf *et al.*, *J. Instrum.* **17**, C03012 (2022).
- <sup>18</sup>O. P. Ford, L. Vanó, J. A. Alonso, J. Baldzuhn, M. N. A. Beurskens, C. Biedermann, S. A. Bozhnikov, G. Fuchert, B. Geiger, D. Hartmann *et al.*, *Rev. Sci. Instrum.* **91**, 023507 (2020).
- <sup>19</sup>N. A. Pablant, M. Bitter, L. Delgado-Aparicio, M. Goto, K. W. Hill, S. Lazerson, S. Morita, A. L. Roquemore, D. Gates, D. Monticello *et al.*, *Rev. Sci. Instrum.* **83**, 083506 (2012).
- <sup>20</sup>N. A. Pablant, R. E. Bell, M. Bitter, L. Delgado-Aparicio, K. W. Hill, S. Lazerson, and S. Morita, *Rev. Sci. Instrum.* **85**, 11E424 (2014).
- <sup>21</sup>s.-l. d. B. L. 2007 2023, “Gaussian processes,” [https://scikit-learn.org/stable/modules/gaussian\\_process.html](https://scikit-learn.org/stable/modules/gaussian_process.html), 2023; accessed November 2023.
- <sup>22</sup>A. Langenberg, J. Svensson, O. Marchuk, G. Fuchert, S. Bozhnikov, H. Damm, E. Pasch, A. Pavone, H. Thomsen, N. A. Pablant *et al.*, *Rev. Sci. Instrum.* **90**, 063505 (2019).
- <sup>23</sup>M. Beurskens, S. Bozhnikov, O. Ford, P. Xanthopoulos, A. Zocco, Y. Turkin, A. Alonso, C. Beidler, I. Calvo, D. Carralero *et al.*, *Nucl. Fusion* **61**, 116072 (2021).
- <sup>24</sup>O. Ford, M. Beurskens, S. Bozhnikov, S. Lazerson, L. Vanó, A. Alonso, J. Baldzuhn, C. Beidler, C. Biedermann, R. Burhenn *et al.*, *Nucl. Fusion* **64**, 086067 (2024).
- <sup>25</sup>F. Warmer, K. Tanaka, P. Xanthopoulos, M. Nunami, M. Nakata, C. D. Beidler, S. A. Bozhnikov, M. N. A. Beurskens, K. J. Brunner, O. P. Ford *et al.*, *Phys. Rev. Lett.* **127**, 225001 (2021).
- <sup>26</sup>K. K. Kirov, F. Leuterer, G. V. Pereverzev, F. Rytter, W. Suttrop, and A. U. team, *Plasma Phys. Controlled Fusion* **44**, 2583 (2002).
- <sup>27</sup>Y. Feng, M. Jakubowski, R. König, M. Krychowiak, M. Otte, F. Reimold, D. Reiter, O. Schmitz, D. Zhang, C. Beidler *et al.*, *Nucl. Fusion* **61**, 086012 (2021).
- <sup>28</sup>T. Klinger, T. Andreeva, S. Bozhnikov, C. Brandt, R. Burhenn, B. Buttenschön, G. Fuchert, B. Geiger, O. Grulke *et al.*, *Nucl. Fusion* **59**, 112004 (2019).
- <sup>29</sup>L. Onsager, *Phys. Rev.* **37**, 405 (1931).
- <sup>30</sup>W. I. van Rij and S. P. Hirshman, *Phys. Fluids B* **1**, 563 (1989).
- <sup>31</sup>P. Helander and A. N. Simakov, *Phys. Rev. Lett.* **101**, 145003 (2008).
- <sup>32</sup>P. Helander, C. D. Beidler, T. M. Bird, M. Drevlak, Y. Feng, R. Hatzky, F. Jenko, R. Kleiber, J. H. E. Proll *et al.*, *Plasma Phys. Controlled Fusion* **54**, 124009 (2012).
- <sup>33</sup>D. Hastings, W. Houlberg, and K. Shaing, *Nucl. Fusion* **25**, 445 (1985).
- <sup>34</sup>N. A. Pablant, A. Langenberg, A. Alonso, C. D. Beidler, M. Bitter, S. Bozhnikov, R. Burhenn, M. Beurskens, L. Delgado-Aparicio, A. Dinklage *et al.*, *Phys. Plasmas* **25**, 022508 (2018).
- <sup>35</sup>V. Nemov, S. Kasilov, W. Kernbichler, and M. Heyn, *Phys. Plasmas* **6**, 4622 (1999).
- <sup>36</sup>M. Yokoyama, H. Maaßberg, C. Beidler, V. Tribaldos, K. Ida, T. Estrada, F. Castejon, A. Fujisawa, T. Minami, T. Shimosuma *et al.*, *Nucl. Fusion* **47**, 1213 (2007).
- <sup>37</sup>R. Kleiber, M. Borchardt, R. Hatzky, A. Könies, H. Leyh, A. Mishchenko, J. Riemann, C. Slaby, J. García-Regaña, E. Sánchez, and M. Cole, *Comput. Phys. Commun.* **295**, 109013 (2024).
- <sup>38</sup>M. Kuczyński, R. Kleiber, H. Smith, C. Beidler, M. Borchardt, J. Geiger, and P. Helander, *Nucl. Fusion* **64**, 046023 (2024).
- <sup>39</sup>J. Ongena, D. Castano-Bardawil, K. Crombé, Y. Kazakov, B. Schweer, I. Stepanov, M. Van Schoor, M. Vervier, A. Krämer-Flecken, O. Neubauer *et al.*, *Fusion Eng. Des.* **192**, 113627 (2023).
- <sup>40</sup>O. Vollmer, A. Stabler, J. Feist, K. Freudenberger, B. Heinemann, H. Lohnert, S. Obermayer, R. Riedl, W. Scharich, E. Speth *et al.*, in *15th IEEE/NPSS Symposium. Fusion Engineering* (IEEE, 1993), Vol. 1, pp. 451–454.
- <sup>41</sup>N. Rust, B. Heinemann, B. Mendelevitch, A. Peacock, and M. Smirnow, *Fusion Eng. Des.* **86**, 728 (2011), part of Special Issue: proceedings of the 26th Symposium of Fusion Technology (SOFT-26).
- <sup>42</sup>W. Ott, E. Speth, and A. Stäbler, “Slowing-down of fast ions in a plasma: Energy transfer, charge exchange losses and wall sputtering,” Technical Report, Max-Planck-Institut für Plasmaphysik, 1977.
- <sup>43</sup>S. Bannmann, O. Ford, U. Hoefel, P. Poloskei, A. Pavone, S. Kwak, J. Svensson, S. Lazerson, P. McNeely, N. Rust *et al.*, *J. Instrum.* **18**, P10029 (2023).
- <sup>44</sup>S. Bannmann, O. Ford, P. Poloskei, J. Svensson, S. Lazerson, and H. Smith, *DPG-Frühjahrstagung 2024* (Deutsche Physikalische Gesellschaft e.V., 2024).
- <sup>45</sup>S. A. Lazerson, O. P. Ford, C. Nuehrenberg, S. Äkäslompolo, P. Z. Poloskei, M. Machielsen, P. McNeely, L. Vanó, N. Rust, S. Bozhnikov *et al.*, *Nucl. Fusion* **60**, 076020 (2020).
- <sup>46</sup>J. Gao, Y. Liu, W. Li, Z. Cui, Y. Dong, J. Lu, Z. Xia, P. Yi, and Q. Yang, *Rev. Sci. Instrum.* **85**, 043505 (2014).
- <sup>47</sup>D. Zhang, R. Burhenn, C. Beidler, Y. Feng, H. Thomsen, C. Brandt, S. Buller, F. Reimold, P. Hacker *et al.*, *Nucl. Fusion* **61**, 116043 (2021).